High-Performance Li–SeS$_x$ All-Solid-State Lithium Batteries

Xiaona Li, Jianwen Liang, Jing Luo, Changhong Wang, Xia Li, Qian Sun, Ruying Li, Li Zhang, Rong Yang, Shigang Lu, Huan Huang, and Xueliang Sun*

All-solid-state Li–S batteries are promising candidates for next-generation energy-storage systems considering their high energy density and high safety. However, their development is hindered by the sluggish electrochemical kinetics and low S utilization due to high interfacial resistance and the electronic insulating nature of S. Herein, Se is introduced into S cathodes by forming SeS$_x$ solid solutions to modify the electronic and ionic conductivities and ultimately enhance cathode utilization in all-solid-state lithium batteries (ASSLBs). Theoretical calculations confirm the redistribution of electron densities after introducing Se. The interfacial ionic conductivities of all achieved SeS$_x$–Li$_3$PS$_4$ (x = 3, 2, 1, and 0.33) composites are 10^{-6} S cm^{-1}. Stable and highly reversible SeS$_x$ cathodes for sulfide-based ASSLBs can be developed. Surprisingly, the SeS$_2$/Li$_{10}$GeP$_2$S$_{12}$–Li$_3$PS$_4$/Li solid-state cells exhibit excellent performance and deliver a high capacity over 1100 mAh g^{-1} (98.5% of its theoretical capacity) at 50 mA g^{-1} and remained highly stable for 100 cycles. Moreover, high loading cells can achieve high areal capacities up to 12.6 mAh cm^{-2}. This research deepens the understanding of Se–S solid solution chemistry in ASSLB systems and offers a new strategy to achieve high-performance S-based cathodes for application in ASSLBs.

All-solid-state lithium batteries (ASSLBs) are attracting tremendous research interests as one of the most promising candidates for next-generation energy storage systems.[1] High energy density and high safety are the primary attractive factors. The use of nonflammable solid electrolytes is a particular advantage over the state-of-the-art Li-ion batteries (LIBs). Considering cathodes for ASSLBs, S is highly favorable due to its large abundance, low cost, low toxicity, and ultrahigh theoretical capacity (1675 mAh g^{-1}). Meanwhile, the lithium polysulfide intermediates, Li$_2$S$_n$ ($4 \leq n \leq 8$), are absent from the solid-solid reaction

mechanism of ASSLBs, which fundamentally eliminates the concern of serious shuttling effects in conventional liquid electrolyte–based Li–S batteries.[2] Among solid-state electrolytes (SSEs), sulfide SSEs (e.g., Li$_{10}$GeP$_2$S$_{12}$ of 1.2×10^{-2} S cm^{-1},[3] Li$_7$P$_3$S$_{11}$ of 1.7×10^{-2} S cm^{-1},[4] and Li$_{9.54}$Si$_{1.74}$P$_{1.44}$S$_{11.7}$Cl$_{0.3}$ of 2.5×10^{-2} S cm^{-1}[5]) have achieved the highest ionic conductivities of $\approx 10^{-2}$ S cm^{-1}, as comparable to liquid electrolytes. The combination of S or Li$_2$S cathodes with sulfide SSEs is also advantageous for their good compatibility in ASSLBs, unlike typical oxide cathodes (such as LiCoO$_2$ and LiNi$_{1/3}$Co$_{1/3}$Mn$_{1/3}$O$_2$) that readily form a space charge layer upon contact with sulfide SSEs and passivate cathode/SSE interface.[6,7]

ASSLBs based on sulfide SSEs and S-containing cathodes were first proposed in the 2000s by Kobayashi et al. using a mixture of Cu$_2$S and S composites as active cathode material.[8] In order to construct pathways for Li$^+$ and electrons, SSEs and various kinds of conductive carbons (such as acetylene black,[9–11] Ketjen Black,[10] activated carbon,[10,12] and reduced graphene oxide[13]) are usually added to the cathode composites. Ball milling is a common method to prepare the composites for its effectiveness in achieving intimate contacts between the cathode components.[14] Nonetheless, good physical contacts between these components cannot guarantee smooth and fast transport of Li$^+$ ions and electrons between the inorganic sulfide SSEs and active particle. The interfacial ionic conductivities are usually poor because of the insulating nature of S and Li$_2$S. Although extensive efforts have been made to improve either electronic or ionic conductivity of the S-based cathodes in ASSLBs,[15–17] the S-based cathodes are still plagued by main challenges of sluggish electrochemical reaction kinetics, low utilization, and low loading of S.

In order to further achieve high electrochemical reaction kinetics of the S-based cathodes in ASSLBs, improvements of ionic and electronic conductivities for the S-based electrochemical active material are crucial. Based on solid solution chemistry, the structural and physicochemical properties of a uniform mixture of substances in solid form can be fine-tuned between the constituents by adjusting their relative proportions. For instance, the bandgap of a solid solution of A and B can be controlled to a value between those of pure A and pure B depending on the composition. Properties of the solid

Dr. X. Li, Dr. J. Liang, J. Luo, C. Wang, Dr. X. Li, Dr. Q. Sun, Dr. R. Li, Prof. X. Sun
Department of Mechanical and Materials Engineering
University of Western Ontario
1151 Richmond St, London, Ontario N6A 3K7, Canada
E-mail: xsun9@uwo.ca
Dr. L. Zhang, Dr. R. Yang, Dr. S. Lu
China Automotive Battery Research Institute Co. Ltd
5th Floor, No. 43, Mining Building, North Sanhuan Middle Road, Beijing 100088, China
Dr. H. Huang
Glabat Solid-State Battery Inc.
700 Collip Circle, London, Ontario N6G 4X8, Canada

The ORCID identification number(s) for the author(s) of this article can be found under https://doi.org/10.1002/adma.201808100.

**ADVANCED
SCIENCE NEWS**

www.advancedsciencenews.com

**ADVANCED
MATERIALS**

www.advmat.de

solution alter correspondingly. This is a particular advantage of solid solutions for designing functional materials with desired properties, offering a strategy to prepared S-based cathodes with controllable electronic conductivity. For example, previous reports have indicated that SeS_x solid solutions can exhibit a high electrochemical performance in liquid lithium battery systems.[18,19] One of the most fascinating features is that the electronic conductivity of a SeS_x solid solution could be improved compared to pure S due to the substantially higher electronic conductivity of Se than S (1×10^{-3} vs 0.5×10^{-27} S m^{-1} at room temperature).[20,21] Unlike conventional Li-ion batteries with liquid electrolytes that can easily wet the electrodes and ensure effective electrochemical reactions, the built-in ionic and electronic conductivities of solid-state electrodes in ASSLBs are very important. Besides the modulation of electronic conductivity, the interfacial ionic conductivity between electrolyte and active materials can also be improved using SeS_x solid solution as the cathode in ASSLSBs. First of all, Se has the excellent compatibility with sulfide-based electrolytes since the chemical similarity between Se and S.[22] Moreover, introducing Se atom into sulfide-based electrolytes could effectively enhance the ionic conductivity and related properties.[23–27] The resulting softening of the electrolyte structures was demonstrated to reduce both the activation barrier for Li$^+$ migration and Arrhenius prefactor.[24,25] However, the use of solid solution chemistry to tailor the electronic or ionic conductivity in ASSLBs is scarce.

Herein, we report for the first time an effective strategy to achieve high utilization of S cathode in ASSLBs by introducing Se to form SeS_x solid solutions. After ball milling with a commercial Li_3PS_4 electrolyte, both the electronic and ionic conductivities of SeS_x–Li_3PS_4 composites could be tailored. Density functional theory (DFT) calculations together with direct current electronic conductivity analyses proved the electronic change when introducing Se into the cathode system. Electrochemical impedance spectra tests were further conducted to reveal the corresponding influence on ionic conductivities. Bilayer SSEs with Li_3PS_4 (on the anode side) and $Li_{10}GeP_2S_{12}$ (on the cathode side) were used as separator between cathode and Li anode to improve electrochemical stability.[28] Among a series of ASSLBs with different SeS_x, the $SeS_2/Li_{10}GeP_2S_{12}$–Li_3PS_4/Li solid state cells exhibited a high capacity over 1100 mAh g^{-1} (98.5% of its theoretical capacity) at 50 mA g^{-1}, good rate capability of 887 mAh g^{-1} at 1 A g^{-1}, and stable cycling performance over 100 cycles. Moreover, the high SeS_2 loading cell could deliver a reversible capacity of 12.6 mAh cm^{-2}, which is among the highest capacities of the state-of-the-art of ASSLBs.[29] Thus, tuning the ionic and electronic conductivities of S-based cathodes based on solid solution chemistry is an important and effective strategy to realize high-energy ASSLB systems.

Density functional theory calculations were performed to theoretically investigate the effects of Se substitution in S_8 molecule. In order to reveal the detailed chemical behaviors of Se_nS_{8-n} ($n = 0,1,2, ..., 8$) rings, a total of 30 possible molecular structures from S_8 to Se_8 with different ratios of Se to S and different positions of Se atoms in the ring of Se_nS_{8-n} were systematically calculated (Figures S1–S10, Supporting Information). The electron density distributions of the S_8 ring and Se_nS_{8-n} rings are similar, presumably due to the similar chemical properties between S and Se. After Se substitution, the electron

density of a Se_nS_{8-n} ring is slightly redistributed compared to the S_8 ring, where the electron cloud tends to migrate from Se to S. Typically, the electron density distributions of S_8 ring and $ortho$-Se_2S_6 ring are compared in **Figure 1**a,b. Based on the higher p orbital and lower electronegativity of Se atom than those of S, Se substitution in the S_8 ring can induce more density of states in the electronic structure of S atoms. Thus, S atoms gain more electron densities in a Se_nS_{8-n} ring compared to the pristine S_8 ring, leading to electronic conductivity of the product. The total energies and related chemical formation energies (ΔE_f's) of different Se_nS_{8-n} rings were summarized in Table S1 (Supporting Information). The ΔE_f's of S_8 and Se_8 rings are −2.039 and −2.270 eV, respectively. There are several Se_nS_{8-n} combinations with different arrangements of atoms. Some of them show lower ΔE_f's than S_8 and Se_8 rings (marked with the red color in Table S1 in the Supporting Information), suggesting they are more stable and should be formed prior to others. As shown in Table S1 (Supporting Information), all of the Se_nS_{8-n} rings with a low ΔE_f are related to the aggregation of Se atoms in the ring. The isolated Se occupation within the ring of Se_nS_{8-n} (with more −S−Se−S− bonds) exhibits higher ΔE_f. As a conclusion, the formation of Se_nS_{8-n} rings would be realized, but most abundant species should be those with Se atoms aggregate together. Basically, the calculation results are consistent well with a previous report.[30,31] The same conclusion can also be drawn from the analyses of SeS_x crystals in the Inorganic Crystal Structure Database (ICSD). For example, a S-rich Se_xS_{1-x} ($Se_{1.1}S_{6.9}$, JCPDS Card No. 01-074-0860) structure exhibits occupation of Se in half of the S_8 ring as well as some Se aggregation in Se_nS_{8-n} rings (Figure S11 and Table S2, Supporting Information). The Se-rich Se_xS_{1-x} ($Se_{3.02}S_{4.98}$, JCPDS Card No. 01-071-0296) structure also reveals the aggregation of Se occupation in Se_nS_{8-n} rings (Figure S12 and Table S3, Supporting Information). Moreover, the existence of those Se_nS_{8-n} rings with lower ΔE_f's than S_8 and Se_8 rings demonstrates the possibility of reversible formation of those Se_nS_{8-n} rings after delithiation process. Based on this, using Se_nS_{8-n} molecules as cathodes in S-based ASSLBs are expected to achieve reversible lithiation/delithiation and electrochemical performance featuring high electronic kinetics. Meanwhile, the aggregation of Se atoms in the Se_nS_{8-n} rings suggests a multistep reaction process, which are related to the S−S, Se−Se, and Se−S bonds in the Se_nS_{8-n} rings. Typically, the calculated bond breaking and lithiation energies (ΔU's) of S−S, S−Se, and Se−Se bonds in the $ortho$-Se_2S_6 rings are −663.85, −614.04, and −607.115 kJ mol^{-1}, respectively (Figure 1c). Whether or not the energy differences can be reflected by the practical lithiation/delithiation processes of SeS_x cathodes in practical ASSLBs remained to be justified.

The SeS_x solid solutions ($x = 3, 2, 1$, and 0.33, corresponding to Se_2S_6, SeS_2, Se_4S_4, and Se_6S_2) were prepared via a typical comelting method based on the S–Se binary phase diagram.[19] The molten Se and S became miscible at 450 °C and formed a uniform solution in a sealed quartz tube. After natural cooling to room temperature, SeS_x solid solutions with different molar ratios were obtained. Corresponding colors of those SeS_x products became thicker from yellow to ruby red to dark brown with increasing Se content (Figure S13, Supporting Information). It should be noted that those SeS_x solid solutions contain a series
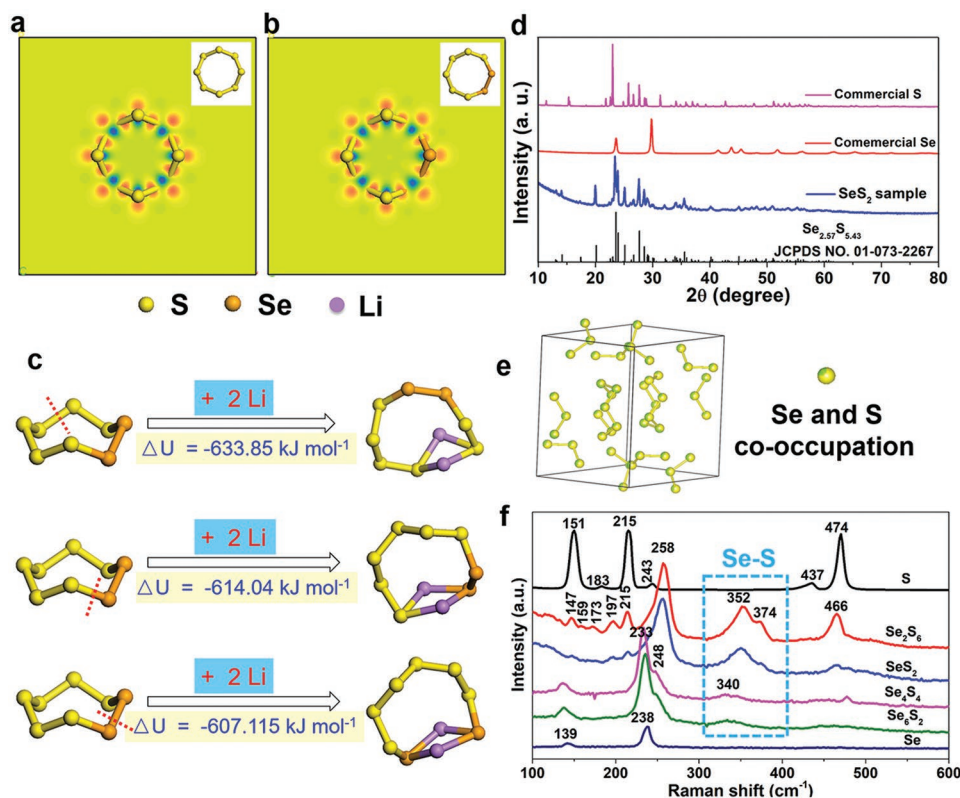
Figure 1. a,b) Electron densities of S_8 (a) and Se_2S_6 (b) rings. c) DFT calculations for the bond breaking and lithiation reaction of the Se_2S_6 ring and proposed intermediates. Orange, yellow and purple stands for Se, S, and Li atoms, respectively. d) XRD patterns of commercial S, Se, and as-prepared SeS_2. e) The structure of $Se_{2.57}S_{5.43}$. f) Raman spectra for S, Se, and as-prepared Se_2S_6, SeS_2, Se_4S_4, and Se_6S_2.

of isomers of Se_nS_{8-n} ring molecules with variable number n and different occupations of Se and S due to the minor ΔE_f difference together with the similarities in electronic structures as shown in Figures S1–S12 (Supporting Information). X-ray diffraction (XRD) was first employed to reveal the reaction and formation of SeS_x solid solutions. As shown in Figure 1d, the reaction between S and Se formed a typical structure of SeS_x solid solution similar to the crystalline $Se_{2.57}S_{5.43}$ (JCPDS No. 01-073-2267). Corresponding structure of $Se_{2.57}S_{5.43}$ is shown in Figure 1e, with all atom sites in the Se_nS_{8-n} rings co-occupied by Se and S. And the only difference is the ratio of S to Se at each site. Other synthesized SeS_x solid solutions also exhibited similar XRD patterns as SeS_2 (Figure S14, Supporting Information) but with slightly varied peak intensities. The XRD analysis confirmed the formation of SeS_x solid solutions rather than simple physical mixtures of Se and S. Furthermore, typical ^{77}Se nuclear magnetic resonance (NMR) spectrum of as-prepared SeS_2 sample in Figure S15 (Supporting Information) clearly confirmed the existence of three groups: Se atom bonding with two S neighbors (≥690 ppm), Se atom bonding with one Se and one S atoms (620–690 ppm), and Se atom bonding with two Se neighbors (≤620 ppm).[32]

Raman spectra of the as-prepared SeS_x solid solutions are also shown in Figure 1f. This figure also includes the spectra of commercial S and Se for comparison. For commercial S, the peaks centered at 151215/474 and 243/437 cm^{-1} are assigned to E_2, A_1, and E_3 symmetry species of S—S bonds.[33,34] For

commercial Se, the two peaks at 139 and 238 cm^{-1} correspond to E and A_1 modes of trigonal Se, respectively.[35] Different from pristine S and Se, additional features highlighting Se–S interactions were observed in the SeS_x solid solutions, as consistent with previous reports.[31,36–38] The peaks near 350 cm^{-1} were assigned to Se–S stretching vibrations. Notably, however, the two Se-rich samples (Se_4S_4 and Se_6S_2) exhibited similar Raman spectra, while the two S-rich samples (Se_2S_6 and SeS_2) shared another set of similar features. For the S-rich samples, the peaks below 220 cm^{-1} arose from the skeleton deformations of the Se_nS_{8-n} ring systems. The peak centered at 466 cm^{-1} associated with S–S stretching modes was also slightly shifted from 474 cm^{-1} of pure S_8 upon introduction of Se.[36,38]

To achieve a uniform physical contact among of the active component, sulfide electrolyte, and conductive carbon additive within the S-based cathodes for ASSLBs, the most popular method is ball milling these components at appropriate molar ratio.[13,15,17,39] The ball-milling method was adopted here to prepare cathode composites for ASSLBs evaluations. The Raman spectra of resulting SeS_x–Li_3PS_4 (SeS_x–LPS, mass ratio 1:1) and SeS_x–Li_3PS_4–C (SeS_x–LPS–C, mass ratio 1:1:0.5, typical scanning electron microscopy (SEM) images in Figure S16 in the Supporting Information) are shown in Figure S17 (Supporting Information). The spectra of SeS_x–LPS composites maintained most characteristic peaks of the SeS_x solid solutions and showed an additional peak at ≈416 cm^{-1} corresponding to fingerprint of PS_4^{3-} unit of Li_3PS_4 solid
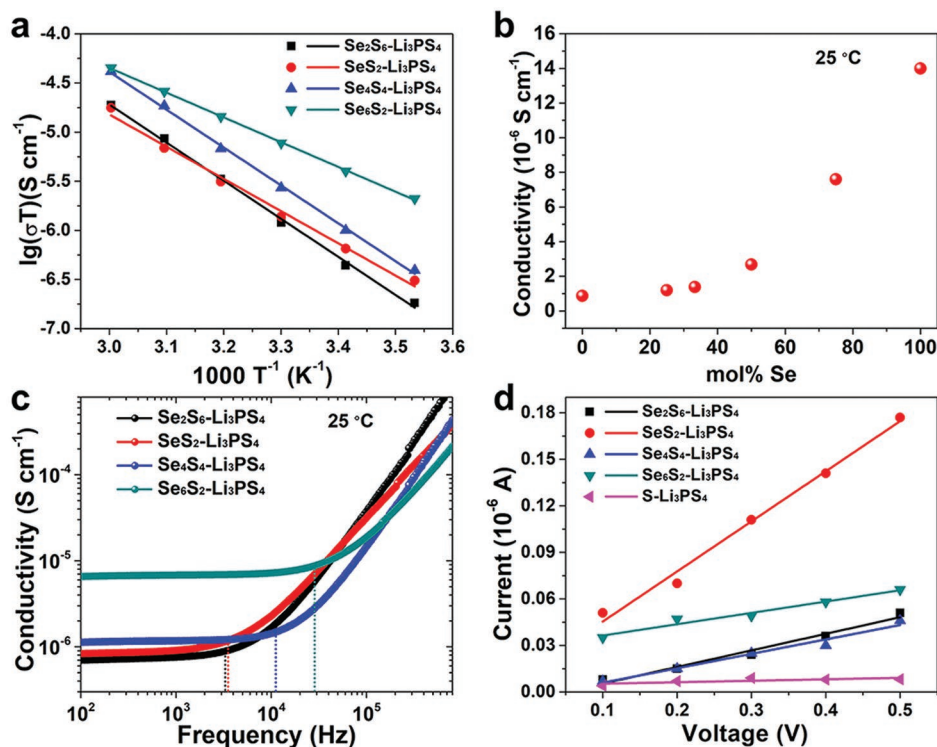
Figure 2. a) Arrhenius plots of AC conductivities of the four SeS$_x$–LPS composites. b) The relationship between ionic conductivities and Se contents in SeS$_x$–LPS at 25 °C. c) The real part of the AC conductivities for the four SeS$_x$–LPS composites at 25 °C. Dashed vertical lines indicate the location of the AC–DC crossover frequency v_H. d) Equilibrium current response of the four SeS$_x$–LPS composites and S–LPS composite at 25 °C at different applied voltages.

electrolyte.[40,41] The ball-milling process with Li$_3$PS$_4$ caused a slightly peak shift, from the original peak at 258 cm^{-1} of Se$_2$S$_6$ and SeS$_2$ to 256 cm^{-1}, and the original peak at 248 cm^{-1} of Se$_4$S$_4$ and Se$_6$S$_2$ to 250 cm^{-1}, along with variations in intensity. These minor changes of Raman features may be due to the interactions between SeS$_x$ solid solutions and Li$_3$PS$_4$, with interfacial species of PS$_{4-x}$Se$_x$$^{3-}$ probably formed.[22] When carbon was added during the ball-milling process, the Raman peak for Li$_3$PS$_4$ was weakened.

To study the ionic and electronic properties of the SeS$_x$ cathodes, SeS$_x$–LPS composites were selected for evaluation to exclude the effects of carbon additive. The temperature-dependent AC conductivities of all four SeS$_x$–LPS composites obtained from the electrochemical impedance spectra (EIS) measurements using symmetric In/SeS$_x$–LPS/In cells are shown in **Figure 2** and Figures S18 and S19 (Supporting Information). In comparison, the ionic conductivities of ball-milled commercial Li$_3$PS$_4$ were also shown in Figure S20 (Supporting Information), which was about 2.6×10^{-4} S cm^{-1} at 25 °C. The higher molar content of Se in the SeS$_x$–LPS composites results in an increased ionic conductivity as observed in Figure 2a,b. Especially, there was a dramatic jump in ionic conductivity when the molar content of Se increased beyond 50%. The numerical values of ionic conductivities at 25 and 60 °C and activation energies (E_a's) are summarized in Table S4 (Supporting Information). The ionic conductivities of all SeS$_x$–LPS composites are as high as 10^{-6} S cm^{-1} at 25 °C. Although these values are lower than pure ball-milled Li$_3$PS$_4$, they are

comparable with some of the reported sulfide SSEs[42] and are also significantly higher than the S–Li$_3$PS$_4$ (S–LPS) counterpart in the same conditions.[22] Generally, the results are consistent with the recent reports about Se introduction into sulfide SSEs, such as Li$_2$S–P$_2$S$_5$–P$_2$Se$_5$,[23] Li$_2$S–Ga$_2$Se$_3$–GeSe$_2$ glasses,[24] and Na$_3$PS$_x$Se$_{4-x}$.[25,26] These reported sulfoselenide solid electrolytes demonstrated "mixed anions" and a softer structure compared to the sulfide electrolytes without Se.[24,26] Same as the effect of introducing Se into those sulfide SSEs, it is supposed that similar influence would also be achieved in the obtained SeS$_x$–LPS composites by softening the structure due to higher higher polarizability of Se.[22] Further benefiting from the formation of interfacial species of PS$_{4-x}$Se$_x$$^{3-}$, the Li$^+$ migration of all SeS$_x$–LPS composites is easier than the S–LPS counterpart. However, even though the ionic conductivities of the SeS$_x$–LPS composites monotonically increase with increasing Se content, the corresponding E_a's do not follow the same trend.

Additional information about the dynamical process of Li$^+$ migration could be further analyzed by the real part of the AC conductivity tests (Figure 2c). There are mainly three types of Li$^+$ migration in the SeS$_x$–LPS composites, including short-time, intermediate-time, and long-time scales migration. The short-time Li$^+$ dynamics, featured by back-and-forth motions over limited ranges, are corresponding to the dispersive conductivity at high frequencies. The long-time Li$^+$ dynamics, featured by random walks resulting in long-range Li$^+$ transport, is corresponding to the conductivity at low frequencies.
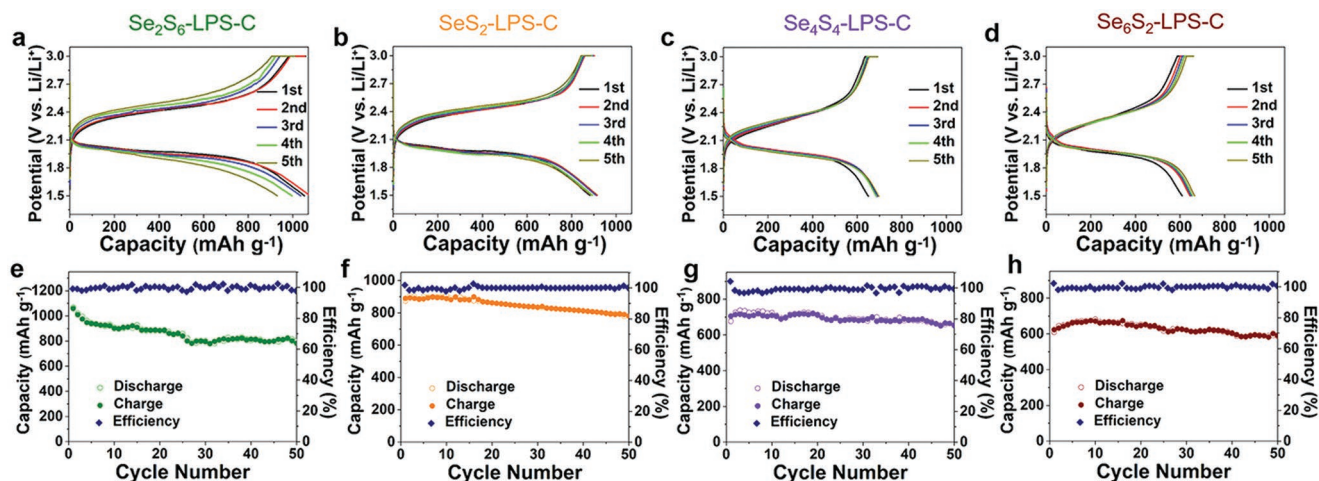
ADVANCED
SCIENCE NEWS
www.advancedsciencenews.com

ADVANCED
MATERIALS
www.advmat.de

Figure 3. Electrochemical performance of SeS_x–LPS–C cathodes at 25 °C. a–d) Discharge–charge curves of cells with: a) Se_2S_6–LPS–C, b) SeS_2–LPS–C, c) Se_4S_4–LPS–C, and d) Se_6S_2–LPS–C cathodes at 50 mA g^{-1}. e–h) Cycling performance and Coulombic efficiencies of the SeS_x–LPS–C cathodes at 25 °C.

Therefore, the high-frequency region should reflect the Li$^+$ migration at the SeS_x/LPS interface. The conductivity spectra is widely described by the Jonscher expression

$$\sigma(v_H) = \sigma_{dc}[1 + (v/v_H)^\alpha], \ (0 \leq \alpha \leq 1) \quad (1)$$

where α is a dimensionless constant and v_H is the frequency marking the onset of frequency-dependent AC conductivity, with the value of $\sigma(v_H) = 2\sigma_{dc}$.[24,43,44] The value of crossover frequency v_H also reflects the time required for Li$^+$ migration within the SeS_x–LPS composites to overcome the percolation barrier in the energy landscape. It is obvious that the Se-rich Se_6S_2–LPS and Se_4S_4–LPS composites exhibit much higher v_H values than those of the S-rich SeS_2–LPS and Se_2S_6–LPS composites, indicating the relatively faster Li$^+$ migration in the same direction. The real part of the AC conductivities for the four SeS_x–LPS composites at different temperatures are also shown in Figure S21 (Supporting Information).

Figure 2d shows the current response of the four SeS_x–LPS composites and S–LPS composite with different applied voltages at room temperature, which were also measured with the symmetric cells using In foil as a current collector. Generally, the equilibrium current increased proportionally to the applied voltage. And the corresponding detailed current-voltage responses as a function of time for the four SeS_x–LPS composites are shown in Figure S22 and Table S4 (Supporting Information). Upon the applied voltage, the cell required an instantly large current to reach the set voltage, followed by a rapid drop and gradual approach to an equilibrium current that was required to hold the voltage. The current response in the initial stage was related to both Li$^+$ and electron transports, while the equilibrium current was mainly attributed to the electronic current since the blocking of Li$^+$ flux. The direct current (DC) electronic conductivities ($\sigma_{dc\text{-}electron}$) of the four SeS_x–LPS composites were calculated and tabulated in Table S5 (Supporting Information). To our surprise, the $\sigma_{dc\text{-}electron}$ values did not increase monotonically with the increase of Se content in the SeS_x–LPS composites. The SeS_2–LPS composite exhibited the highest $\sigma_{dc\text{-}electron}$ of 2.55×10^{-8} S cm^{-1} calculated based

on DC method.[45,46] Nevertheless, all of the $\sigma_{dc\text{-}electron}$ values for the SeS_x–LPS composites were much higher than those of S–LPS composites. Improvement of both ionic and electronic conductivities by introduction of Se could be concluded. It should be not that the improvement of electronic conductivities is not mainly due to the electronic property of SeS_x when introducing Se, but more rely on the interaction between SeS_x and LPS (detailed discussion see supporting information).

The electrochemical performances of the SeS_x–LPS–C cathodes were evaluated in ASSLBs at 25 °C using Li anode and bilayer $Li_{10}GeP_2S_{12}/Li_3PS_4$ (LGPS/LPS) electrolyte. Here, the bilayer LGPS/LPS electrolyte was prepared by pelletizing 45 mg of LGPS and 45 mg of LPS under 240 MPa based on previous reports to improve the cycling stability.[28,47,48] During the cell assembly, the SeS_x cathodes were directly placed on the LGPS side, and bare Li was directly in contact with the LPS side. The relatively stable battery system was reflected by the time-dependent EIS of the assembled ASSLBs at different states (Figure S23, Supporting Information). Both the reversible capacities and current densities of the cells with the SeS_x–LPS–C cathodes were calculated based on the mass of SeS_x components within the cathodes. And the theoretical capacity of SeS_x is 1225, 1125, 966, and 815 mAh g^{-1}, respectively, for Se_2S_6, SeS_2, Se_4S_4, and Se_6S_2, considering the total conversion to Li_2Se and Li_2S in the discharge state.

Figure 3a–d shows the discharge–charge curves of the ASSLBs with SeS_x–LPS–C cathodes cycled between 1.5 and 3.0 V at 50 mA g^{-1}. During the first five cycles, the Se_2S_6–LPS–C cathode exhibited capacity decay with an obvious increase in polarization of the charge profile. In contrast, the other three SeS_x–LPS–C cathodes displayed relatively stable cycling performance, with almost overlapping discharge–charge curves for the initial cycles. The reversible capacities of the four cathodes at the fifth cycle were 930, 889, 747, and 665 mAh g^{-1} with the increasing of Se content in the SeS_x solid solutions, corresponding to 76%, 79%, 77%, and 82% of their theoretical capacities. The results indicated that the Se component at all ratios in the SeS_x cathodes have contributed to the high utilization of active materials as a result of increased electronic conductivities.

ADVANCED
SCIENCE NEWS
www.advancedsciencenews.com

ADVANCED
MATERIALS
www.advmat.de

More importantly, a higher Se content can lead to a more stable long-term cycling performance as shown in Figure 3e–h. Reversible capacities of 799, 782, 666, and 600 mAh g^{-1} were maintained after 50 cycles for the cathodes with increasing Se contents, corresponding to capacity retentions of 85.9%, 88.0%, 89.2%, and 90.2% (compared to the capacity at the fifth cycle), respectively. The corresponding volumetric capacities calculated based on the densities of active components (SeS$_x$ here) are presented in Figure S24 (Supporting Information). Though the mass capacities of Se$_2$S$_6$–LPS–C and SeS$_2$–LPS–C cathodes are much higher than that of Se$_4$S$_4$–LPS–C and Se$_6$S$_2$–LPS–C cathodes, while the latter two exhibited comparable volumetric capacities. Nonetheless, the higher Se content also results in lower theoretical and practical specific capacities. Therefore, the SeS$_2$ cathode has exhibited both optimized capacity and stability. The corresponding morphologies and elements distribution of the SeS$_2$–LPS–C (pellet) before and after cycling are shown in Figures S25 and S26 (Supporting Information). Slightly increased particle size and interconnection among particles could be observed, which might be due to the volume change of active SeS$_2$ during cycling.

Furthermore, all the SeS$_x$ cathodes exhibited relatively smooth discharge–charge curves without obvious plateaus (Figure 3a–d), so as the galvanostatic intermittent titration technique (GITT) curves at the third cycle (Figure S27, Supporting Information). This phenomenon was slightly different from the predicted "stepwise" lithiation processes based on DFT calculation, which should be due to the close similarity between Se and S. Actually, the typical single-plateau discharge–charge curves could be reasonable for solid-state reactions that omitting the soluble polysulfide or polyselenide intermediates,[21,49,50] but we will discuss more in details in later sections. To evaluate the influence of reaction kinetics of SeS$_x$–LPS–C cathodes during cycling, the Li$^+$ diffusion coefficient (D_{Li}) based on Fick's second law was estimated from GITT are plotted in Figure S27 (Supporting Information).[51] The D_{Li} values for the four cathodes were in the same order of magnitude around 10^{-11} cm^2 s^{-1}, which were compatible with other conversion type cathodes in ASSLBs.[52]

Now the question arises here is that whether the lithiation of those proposed S—S, S—Se, and Se—Se bonds within the SeS$_x$ cathodes could be distinguished in the ASSLB systems. As far as we know, typical S cathodes in ASSLBs exhibit only one plateau corresponding to direct conversion from S to Li$_2$S, rather than the formation of long-chain lithium polysulfide intermediates in ether-based liquid batteries. However, it should be quite different for SeS$_x$ solid solutions in the ASSLBs system, since the potential barrier and energy barrier to promote the lithiation of the three types of bonds (S—S, S—Se, and Se—Se) were proven to be different by DFT calculations.

To facilitate the lithiation/delithiation kinetics of SeS$_x$ cathodes, the four SeS$_x$–LPS–C cathodes were further tested at 60 °C. Evidently, the four cathodes exhibited higher D_{Li} values (**Figure 4**a–d) compared to that at 25 °C. As expected, clearly three discharge plateaus could be seen obviously in the GITT curves (also the third cycle), with a small one around 2.25 V and two dominant plateaus at ≈2.1 and 2.0 V. The three discharge plateaus suggest the stepwise lithiation process, which might be related to the different types of bonds exist within the SeS$_x$ solid

solutions in any desired ratios. Ex situ XRD and X-ray photoelectron spectroscopy (XPS) analysis of the typical SeS$_2$–Li$_3$PS$_4$–C cathode at different discharge–charge states in Figures S28 and S29 (Supporting Information) demonstrates the formation of Li$_2$Se and Li$_2$S at fully discharge state and the reversible of the active SeS$_2$. While it is difficult to verify the recovery state when recharged to 3.0 V exactly, since that the pristine SeS$_x$ with eight-membered ring structure after mixing with commercial Li$_3$PS$_4$ solid electrolyte and carbon might be changed reflected from the Raman (Figure 1f; Figure S17, Supporting Information) and XPS (Figure S29, Supporting Information) data. More detailed mechanism and characterization are being investigated in ongoing studies in our laboratory.

Moreover, slightly capacity increasing in the initial few cycles was observed as shown in Figure 4e,f, and similar behaviors were also observed in other S-based cathodes in ASSLBs,[17,29] which indicated an activation process for the active SeS$_x$ components together with partial lithiation/delithiation of sulfide electrolyte within the cathode composite during cycling (Figure S30, Supporting Information).[29] The reversible capacities obtained at the fifth cycle were 1086, 1116, 883, and 733 mAh g^{-1} for SeS$_x$ solid solutions with increasing Se contents, corresponding to 87%, 99%, 91%, and 90% of the theoretical specific capacities. Consistent with the cycling performance as 25 °C, obvious capacity decay was observed for Se$_2$S$_6$–LPS–C cathode with the highest S content, while relatively stable cycleabilities for other three cathodes with higher Se content. The capacities were 772, 935, 849, and 716 mAh g^{-1} for Se$_2$S$_6$–LPS–C, SeS$_2$–LPS–C, Se$_4$S$_4$–LPS–C, and Se$_6$S$_2$–LPS–C cathodes after 100 cycles, respectively (Figure 4e). Furthermore, the volumetric capacity of Se$_6$S$_2$–LPS–C cathodes was even higher than that of SeS$_2$–LPS–C as shown in Figure S31 (Supporting Information). The improvement of reversible capacity and cycling stability of SeS$_x$–LPS–C cathodes at 60 °C should be due to the much reduced polarization and facilitated electrochemical reaction kinetics, which are guaranteed by improved ionic conductivity of solid electrolyte itself and SeS$_x$–LPS components within the cathode layer. Otherwise, the lithiation/delithiation of the active material would not be completed and some of the active material would be isolated since the sluggish ionic/electronic diffusional pathways at low temperature, resulting the reduced reversible capacity along cycling. Figure 4f and Figure S32 (Supporting Information) show the rate capabilities of the SeS$_x$–LPS–C cathodes over a current density range from 0.2 to 1 A g^{-1}. Apparently, the SeS$_2$–LPS–C cathode exhibited the best rate capability, with highly reversible capacities of 1024, 970, 949, and 887 mAh g^{-1} achieved at 0.2, 0.4, 0.6, and 1 A g^{-1}, respectively. Corresponding capacity retention plots in Figure S33 (Supporting Information) clearly shows that SeS$_x$–LPS–C cathodes with higher Se contents exhibit better rate performance with ≈85% capacity retention at 1 A g^{-1} compared to ≈67% for the Se$_2$S$_6$–LPS–C cathode.

Here, the impact of cathode loading was further investigated to achieve high capacity for ASSLBs. The SeS$_2$–LPS–C cathode was adopted considering its good performance at moderate loading. **Figure 5**a,b displays the discharge–charge curves of SeS$_2$–LPS–C cathode cycled between 1.5 and 3.0 V at 30 mA g^{-1} with total loadings of 25.5 and 38.2 mg cm^{-2} (corresponding to SeS$_2$ loadings of 10.2 and 15.3 mg cm^{-2}), respectively. The

**ADVANCED
SCIENCE NEWS**

www.advancedsciencenews.com

**ADVANCED
MATERIALS**

www.advmat.de
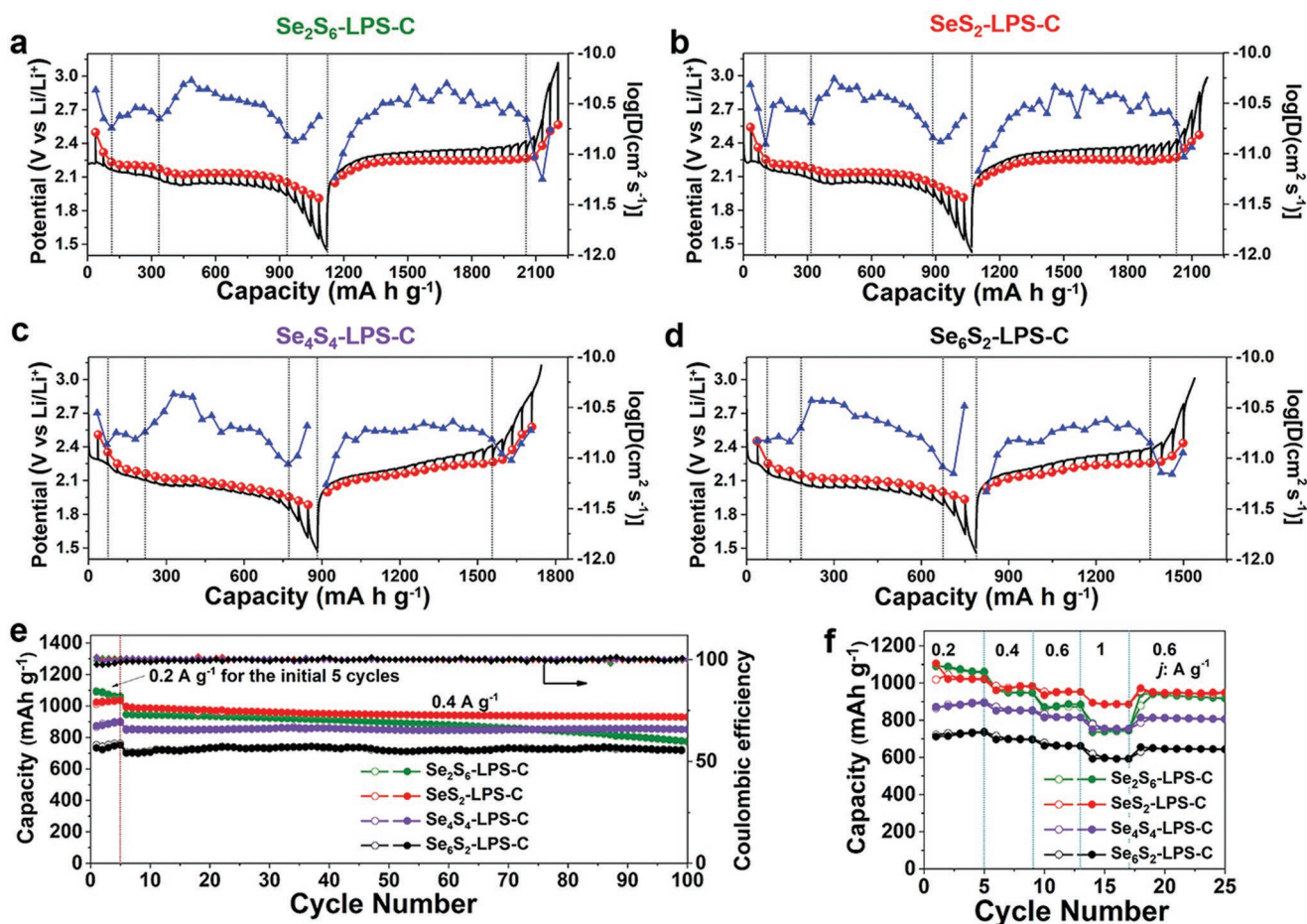
Figure 4. Electrochemical performance of SeS$_x$–LPS–C cathodes at 60 °C. a–d) GITT of SeS$_x$–LPS–C cathodes in the third cycle. 30 mA g^{-1} current pulses are used for 1 h increments followed by a 4 h relaxation. e) Cycling performance of SeS$_x$–LPS–C cathodes at 0.4 A g^{-1}. f) Rate capabilities of SeS$_x$–LPS–C cathodes at different current densities from 0.2 to 1 A g^{-1}.

tests were performed at 60 °C. Both high-loading cells exhibited similar discharge–charge curves compared to that with moderate loading (Figure 4b), and delivered initial discharge capacities of 8.5 and 12.6 mAh cm^{-2} depending on the loading. Moreover, good reversible capacity and cycling stability could be achieved. Upon cycling, the capacity of the highest loading cell maintained a high areal capacity of 11.8 mAh cm^{-2} at the tenth cycle, which is 94% of the initial discharge capacity. To the best of our knowledge, the performance of high-loading cells is among the best reported ASSLBs (Figure 5d).[13,15,22,29,39,53,54] Basically, there are two main reasons for the capacity decay for high loading cells. The first reason is the strain and stress accumulated at the electrode/electrolyte interface and crack formations within the cathode composites due to volume change of the active SeS$_2$. Carbon additives could alleviate partial of the volume change to some extent but cannot solve the problem fundamentally. The second reason is the unsolved interfacial issues between solid electrolyte and Li metal anode.[55] Moreover, the performance of Li metal anodes is highly dependent on the cycling areal capacity. In our case, the capacity of the cell was as high as ≈12 mAh cm^{-2}, which correspond to ≈60 µm of Li metal theoretically. The equivalent amount of Li$^+$ have to migrate from the Li metal anode through the solid electrolyte

and to the cathode during discharge, and a reverse flux is required during charge, which will be leading to the unstable lithium/sulfide electrolyte interface. Actually, such high capacity is still a big challenge for Li metal anode not only in ASSLBs but also in liquid electrolyte based LIBs. There is almost no report with such high capacity for symmetric Li/solid electrolyte/Li cells even with different Li protection approaches.[56–58] Problems of mechanical degradation and electrode/sulfide electrolyte instability in sulfide-based ASSLBs need to be solved for practical applications.

In summary, this work reveals a rational design of SeS$_x$ solid solution cathodes for sulfide solid electrolyte-based ASSLBs. A detailed DFT calculation study was performed to identify the structural and physicochemical properties for different SeS$_x$ solid solutions with variable stoichiometry. DFT calculations suggest that: 1) the redistributed properties in the Se$_n$S$_{8-n}$ rings, 2) preferred aggregation of Se atoms in the Se$_n$S$_{8-n}$ rings, 3) reasonable multilithiation steps for SeS$_x$ electrodes, and 4) possible reformation of SeS$_x$ after delithiaiton process considering the lowest activation energy. Confirmed by experimental results, the ionic and electronic conductivities of the SeS$_x$–Li$_3$PS$_4$–C cathodes can be favorably tuned by the ratio of Se to S. By optimizing the molar ratio between Se and S, SeS$_x$

ADVANCED
SCIENCE NEWS
www.advancedsciencenews.com

ADVANCED
MATERIALS
www.advmat.de

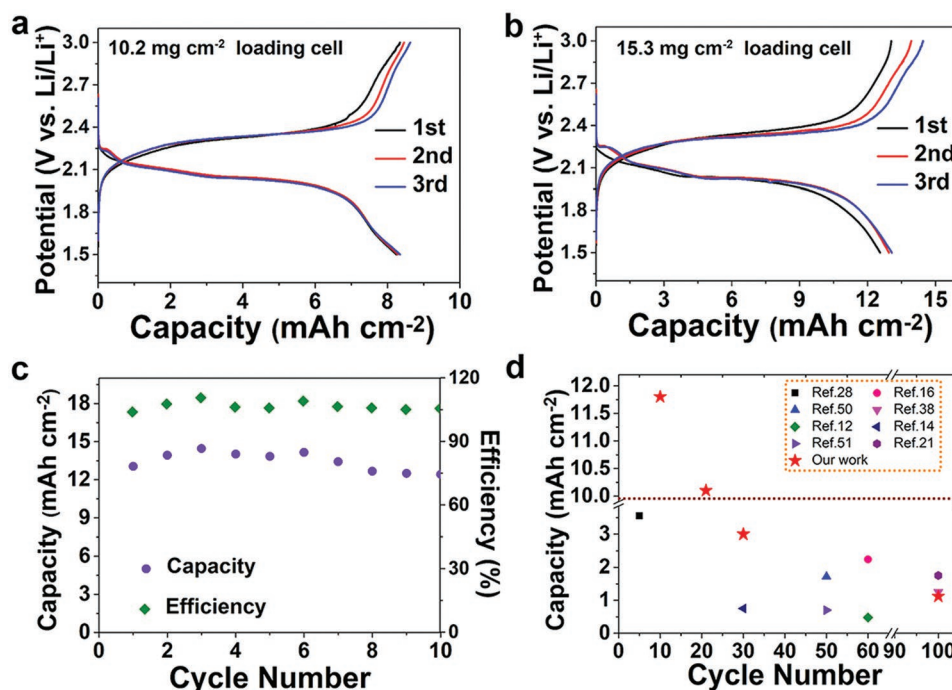**Figure 5.** Electrochemical performance of the SeS_2–LPS–C cathodes with high loading at 60 °C. a,b) Discharge–charge curves of cells with loading of: a) 10.2 mg cm^{-2} and b) 15.3 mg cm^{-2} at 30 mA g^{-1}. c) Cycling performance of the SeS_2–LPS–C cathodes with SeS_2 loading of 15.3 mg cm^{-2}. d) Comparison of the areal capabilities and cycling performance for S-based ASSLBs reported in the literature recently and the results of this work.

cathodes present outstanding electrochemical performance in ASSLBs. In particular, high loading cells with SeS_2 could achieve ultrahigh capacity up to 12.6 mAh cm^{-2}. All these findings extend the conventional knowledge on SeS_x solid solution to ASSLBs system. The significance of cathode ionic/electronic conductivities on electrochemical performance is proved. Modifications based on solid solution chemistry is demonstrated to be an effective strategy for enhancing the built-in properties of S cathodes for future practical implementations in ASSLBs.

Experimental Section

Preparation of Se_2S_6, SeS_2, Se_4S_4, and Se_6S_2 Composites: All chemicals were purchased from Sigma-Aldrich and used directly without further treatment. The SeS_x solid solutions (x = 3, 2, 1, and 0.33, corresponding to Se_2S_6, SeS_2, Se_4S_4, and Se_6S_2) were prepared by comelting commercial selenium and sulfur powders.[19] In a typical synthesis, sulfur and selenium powders with a designed molar ratio were mixed and sealed in a glass tube under vacuum. The sealed glass tube was heated up to 450 °C with a heating rate of 5 °C min^{-1} in a quartz tube and then held at 450 °C for 24 h before cooling back to room temperature naturally.

Preparation of the SeS_x–Li_3PS_4–C (SeS_x–LPS–C) Cathode Composites: The obtained SeS_x powder was mixed with Li_3PS_4 (99.95%, MSE supplies, LLC) and acetylene black (AB) at a weight ratio of 40:40:20 by ball milling for 4 h in Ar atmosphere.

Characterizations: The morphology of all materials was analyzed using Hitachi S-4800 field emission scanning electron microscopy operated at 5 kV. The X-ray diffraction patterns were collected using a Bruker D8 Advance equipped with a Cu Kα source (λ = 0.154 nm) Cu Kα spectrometer under 40 kV and 40 mA. Raman spectra were obtained using a HORIBA Scientific LabRAM HR Raman spectrometer system equipped with a 532.4 nm laser. The static ^{77}Se NMR spectrum of as-prepared SeS_2 sample was measured on a Bruker Avance III

400 spectrometer operating at 400 MHz for ^{77}Se (9.4 T). The X-ray photoelectron spectroscopy measurement was performed on XPS (Krotos AXIS Ultra Spectrometer) system.

DFT Calculations: First-principles computations were performed within the Materials Studio by using the CASTEP DFT code with the exchange-correlation functional of Perdew–Burke–Ernzerhof (PBE) based on generalized gradient approximation (GGA). To reveal the molecular structure, electron density difference and related energy change of the Se_nS_{8-n} (0 ≤ n ≤ 8) rings have been geometrically optimized via DFT calculation. A total of 30 feasible molecular structures from S_8 to Se_8 with different ratios of Se to S and different positions of Se atoms in the Se_nS_{8-n} rings were systematically studied. To identify the chemical formation energy (ΔE_f) of different Se_nS_{8-n} rings, we calculated the total energies of S atom, Se atom, and different Se_nS_{8-n} molecular rings. The chemical formation energy are defined as $\Delta E_f = (\Delta U_{SenS8-n} - \Delta U_{Se} - \Delta U_S)/nF$, where n is the number of electrons transferred in the molecular rings formation and F is the Faraday constant. $\Delta U_{SenS8-n}$, ΔU_{Se}, and ΔU_S were evaluated according to changes in enthalpy at 0 K by total energy calculations of Se_nS_{8-n} rings, Se and S, respectively. ΔE_f is the calculated chemical energy for the formation of possible Se_nS_{8-n} rings. To identify the bond breaking and lithiation energies of S—S, S—Se, and Se—Se bonds in the Se_2S_6 molecular rings, three kinds of feasible $Li_2Se_2S_6$ molecule structures were built based on different bond breaking and lithiation routes for S—S, S—Se, and Se—Se bonds. Those $Li_2Se_2S_6$ molecule structures have been optimized based on the geometry optimization through the DFT calculation. Then, the total energy of Li, Se_2S_6 molecule, and $Li_2Se_2S_6$ molecule structures were calculated. The bond breaking and lithiation energies ΔU's are defined as $\Delta U = (\Delta U_{Li2Se2S6} - \Delta U_{Li} - \Delta U_{Se2S6})$, where $\Delta U_{Li2Se2S6}$, ΔU_{Li} and ΔU_{Se2S6} is evaluated according to changes in enthalpy at 0 K by total energy calculation of $Li_2Se_2S_6$, Li, and Se_2S_6, respectively.

ASSLB Cell Fabrication: To assemble solid state cells, 45 mg of the $Li_{10}GeP_2S_{12}$ (99.95%, MSE supplies, LLC) and 45 mg of Li_3PS_4 were pressed successively at 2 ton inside a poly(tetrafluoroethylene) (PTFE) die to form the bilayer solid electrolyte. 4 mg of the cathode composite

with active SeS_x mass loading about 1.6 mg cm^{-2} was then pressed onto the $Li_{10}GeP_2S_{12}$ electrolyte side at 3 metric ton. Finally, a piece of Li foil was attached on the Li_3PS_4 electrolyte side at 1 ton. For the high cathode loading cells, the active SeS_2 loading ranged between 7.6 and 15.3 mg cm^{-2}, and the assembled cells were tested under applied pressure of 100 MPa during cycling.

All the electrochemical measurements were performed on a Land cycler (Wuhan, China) at room temperature or 60 °C. Electrochemical impedance spectra was obtained with a bias of 20 mV in the frequency range of 1 Hz to 7 MHz. The ionic conductivity tests were carried out at temperatures between 10 and 60 °C. The impedance spectra were fitted using the EC-lab software. The DC electronic conductivities were measured on In/SeS_x–Li_3PS_4/In and In/S–Li_3PS_4/In symmetric cells, with an applied voltage between 0.1 and 0.5 V for 3600 s. The galvanostatic intermittent titration technique measurements were carried out with a pulse current of 30 mA g^{-1} for 1 h and rest for 4 h.

Supporting Information

Supporting Information is available from the Wiley Online Library or from the author.

Conflict of Interest

The authors declare no conflict of interest.

[1] A. Manthiram, X. Yu, S. Wang, *Nat. Rev. Mater.* **2017**, *2*, 16103.
[2] S. Gu, C. Sun, D. Xu, Y. Lu, J. Jin, Z. Wen, *Electrochem. Energy Rev.* **2018**, *1*, 599.
[3] N. Kamaya, K. Homma, Y. Yamakawa, M. Hirayama, R. Kanno, M. Yonemura, T. Kamiyama, Y. Kato, S. Hama, K. Kawamoto, *Nat. Mater.* **2011**, *10*, 682.
[4] Y. Seino, T. Ota, K. Takada, A. Hayashi, M. Tatsumisago, *Energy Environ. Sci.* **2014**, *7*, 627.
[5] Y. Kato, S. Hori, T. Saito, K. Suzuki, M. Hirayama, A. Mitsui, M. Yonemura, H. Iba, R. Kanno, *Nat. Energy* **2016**, *1*, 16030.
[6] W. Zhang, F. Richter, S. P. Culver, T. Leichtweiß, J. G. Lozano, C. Dietrich, P. G. Bruce, W. G. Zeier, J. Janek, *ACS Appl. Mater. Interfaces* **2018**, *10*, 22226.
[7] J. Auvergniot, A. Cassel, J.-B. Ledeuil, V. Viallet, V. Seznec, R. Dedryvère, *Chem. Mater.* **2017**, *29*, 3883.
[8] K. Kobayashi, N. Machida, T. Shigematsu, in *Preprints of Annual Meeting of The Ceramic Society of Japan Preprints of Fall Meeting of The Ceramic Society of Japan 15th Fall Meeting of The Ceramic Society of Japan*, The Ceramic Society of Japan **2002**, p. 409.
[9] J. E. Trevey, J. R. Gilsdorf, C. R. Stoldt, S.-H. Lee, P. Liu, *J. Electrochem. Soc.* **2012**, *159*, A1019.
[10] H. Nagata, Y. Chikusa, *J. Power Sources* **2014**, *264*, 206.
[11] M. Nagao, A. Hayashi, M. Tatsumisago, *J. Mater. Chem.* **2012**, *22*, 10015.
[12] C. Yu, L. van Eijck, S. Ganapathy, M. Wagemaker, *Electrochim. Acta* **2016**, *215*, 93.
[13] R. Xu, Z. Wu, S. Zhang, X. Wang, Y. Xia, X. Xia, X. Huang, J. Tu, *Chem. – Eur. J.* **2017**, *23*, 13950.
[14] M. Nagao, A. Hayashi, M. Tatsumisago, *Electrochim. Acta* **2011**, *56*, 6055.
[15] X. Yao, N. Huang, F. Han, Q. Zhang, H. Wan, J. P. Mwizerwa, C. Wang, X. Xu, *Adv. Energy Mater.* **2017**, *7*, 1602923.
[16] Z. Lin, Z. Liu, N. J. Dudney, C. Liang, *ACS Nano* **2013**, *7*, 2829.
[17] F. Han, J. Yue, X. Fan, T. Gao, C. Luo, Z. Ma, L. Suo, C. Wang, *Nano Lett.* **2016**, *16*, 4521.
[18] A. Abouimrane, D. Dambournet, K. W. Chapman, P. J. Chupas, W. Weng, K. Amine, *J. Am. Chem. Soc.* **2012**, *134*, 4505.
[19] X. Li, J. Liang, K. Zhang, Z. Hou, W. Zhang, Y. Zhu, Y. Qian, *Energy Environ. Sci.* **2015**, *8*, 3181.
[20] A. Eftekhari, *Sustainable Energy Fuels* **2017**, *1*, 14.
[21] G. Xu, J. Liu, R. Amine, Z. Chen, K. Amine, *ACS Energy Lett.* **2017**, *2*, 605.
[22] X. Li, J. Liang, X. Li, C. Wang, J. Luo, R. Li, X. Sun, *Energy Environ. Sci.* **2018**, *11*, 2828.
[23] J. Kim, Y. Yoon, M. Eom, D. Shin, *Solid State Ionics* **2012**, *225*, 626.
[24] M. A. Marple, B. G. Aitken, S. Kim, S. Sen, *Chem. Mater.* **2017**, *29*, 8704.
[25] T. Krauskopf, C. Pompe, M. A. Kraft, W. G. Zeier, *Chem. Mater.* **2017**, *29*, 8859.
[26] S.-H. Bo, Y. Wang, G. Ceder, *J. Mater. Chem. A* **2016**, *4*, 9044.
[27] T. Bernges, S. P. Culver, N. Minafra, R. Koerver, W. G. Zeier, *Inorg. Chem.* **2018**, *57*, 13920.
[28] B. R. Shin, Y. J. Nam, D. Y. Oh, D. H. Kim, J. W. Kim, Y. S. Jung, *Electrochim. Acta* **2014**, *146*, 395.
[29] U. Ulissi, S. Ito, S. M. Hosseini, A. Varzi, Y. Aihara, S. Passerini, *Adv. Energy Mater.* **2018**, *8*, 1801462.
[30] J. Komulainen, R. S. Laitinen, R. Suontamo, *Can. J. Chem.* **2002**, *80*, 1435.
[31] J. Taavitsainen, H. Lange, R. S. Laitinen, *J. Mol. Struct.: THEOCHEM* **1998**, *453*, 197.
[32] R. S. Laitinen, T. A. Pakkanen, *Inorg. Chem.* **1987**, *26*, 2598.
[33] X. Li, J. Liang, Y. Lu, Z. Hou, Q. Cheng, Y. Zhu, Y. Qian, *Angew. Chem., Int. Ed.* **2017**, *56*, 2937.
[34] A. T. Ward, *J. Phys. Chem.* **1968**, *72*, 4133.
[35] X. Li, J. Liang, Z. Hou, W. Zhang, Y. Wang, Y. Zhu, Y. Qian, *Adv. Funct. Mater.* **2015**, *25*, 5229.
[36] R. S. Laitinen, *Acta Chem. Scand.* **1987**, *41a*, 361.
[37] R. Steudel, R. Laitinen, *Inorganic Ring Systems*, Springer, Berlin, Germany **1982**, pp. 177–197.
[38] H. Eysel, S. Sunder, *Inorg. Chem.* **1979**, *18*, 2626.
[39] Y. Zhang, T. Liu, Q. Zhang, X. Zhang, S. Wang, X. Wang, L. Li, L. Fan, C. Nan, Y. Shen, *J. Mater. Chem. A* **2018**, *6*, 23345.
[40] N. H. H. Phuc, K. Morikawa, T. Mitsuhiro, H. Muto, A. Matsuda, *Ionics* **2017**, *23*, 2061.
[41] N. H. H. Phuc, K. Morikawa, M. Totani, H. Muto, A. Matsuda, *Solid State Ionics* **2016**, *285*, 2.
[42] S. Teragawa, K. Aso, K. Tadanaga, A. Hayashi, M. Tatsumisago, *J. Power Sources* **2014**, *248*, 939.

[43] J. C. Dyre, P. Maass, B. Roling, D. L. Sidebottom, *Rep. Prog. Phys.* **2009**, *72*, 046501.

[44] D. Sidebottom, *Rev. Mod. Phys.* **2009**, *81*, 999.

[45] T. Y. Yang, G. Gregori, N. Pellet, M. Grätzel, J. Maier, *Angew. Chem.* **2015**, *127*, 8016.

[46] H. Morimoto, H. Yamashita, M. Tatsumisago, T. Minami, *J. Am. Ceram. Soc.* **1999**, *82*, 1352.

[47] K. H. Park, D. Y. Oh, Y. E. Choi, Y. J. Nam, L. Han, J. Y. Kim, H. Xin, F. Lin, S. M. Oh, Y. S. Jung, *Adv. Mater.* **2016**, *28*, 1874.

[48] D. Y. Oh, Y. E. Choi, D. H. Kim, Y.-G. Lee, B.-S. Kim, J. Park, H. Sohn, Y. S. Jung, *J. Mater. Chem. A* **2016**, *4*, 10329.

[49] S. Xiong, M. Regula, D. Wang, J. Song. *Electrochem. Energy Rev.* **2018**, *1*, 388.

[50] X. Yang, X. Li, K. Adair, H. Zhang, X. Sun, *Electrochem. Energy Rev.* **2018**, *1*, 239.

[51] C. J. Wen, B. Boukamp, R. A. Huggins, W. Weppner, *J. Electrochem. Soc.* **1979**, *126*, 2258.

[52] J. M. Whiteley, S. Hafner, S. S. Han, S. C. Kim, K. H. Oh, S. H. Lee, *Adv. Energy Mater.* **2016**, *6*, 1600495.

[53] K. Suzuki, N. Mashimo, Y. Ikeda, T. Yoko, M. Hirayama, R. Kanno, *ACS Appl. Energy Mater.* **2018**, *1*, 2373.

[54] X. Yao, D. Liu, C. Wang, P. Long, G. Peng, Y. Hu, H. Li, L. Chen, X. Xu, *Nano Lett.* **2016**, *16*, 7148.

[55] L. Porz, T. Swamy, B. W. Sheldon, D. Rettenwander, T. Frömling, H. L. Thaman, S. Berendts, R. Uecker, W. C. Carter, Y. M. Chiang, *Adv. Energy Mater.* **2017**, *7*, 1701003.

[56] Y. Gao, D. Wang, Y. Li, Z. Yu, T. Mallouk, D. Wang, *Angew. Chem., Int. Ed.* **2018**, *57*, 13608.

[57] F. Han, J. Yue, X. Zhu, C. Wang, *Adv. Energy Mater.* **2018**, *8*, 1703644.

[58] M. Suyama, A. Kato, A. Sakuda, A. Hayashi, M. Tatsumisago, *Electrochim. Acta* **2018**, *286*, 158.